Simulation model of Reactive Nitrogen species in an urban atmosphere using a Deep neural network: RNDv1.0

Junsu Gil[1], Meehye Lee[1], Jeonghwan Kim[2], Gangwoong Lee[2], Joonyoung Ahn[3], Cheol-Hee Kim[4]

[1] Department of Earth and Environmental Sciences, Korea University, Seoul, South Korea
[2] Department of Environmental Science, Hankuk University of Foreign Studies, Yongin, South Korea
[3] Air Quality Forecasting Center, Climate and Air Quality Research Department, National Institute of Environmental Research (NIER), Incheon, South Korea
[4] Department of Atmospheric Sciences, Pusan National University, Busan, South Korea

Correspondence to: Meehye Lee (meehye@korea.ac.kr)

Abstract. Nitrous acid (HONO), one of a reactive nitrogen oxide, plays an important role in the formation of ozone and fine aerosols in the urban atmosphere. In this study, a new simulation approach is presented to calculate the HONO mixing ratios using a deep neural technique based on measured variables. The "Reactive Nitrogen species simulation using deep neural network (RND)" is implemented in Python. The first version of RND (RNDv1.0) is trained, validated, and tested with HONO measurement data obtained in Seoul from 2016 to 2021. RNDv1.0 is constructed using k-fold cross validation and evaluated with index of agreement, correlation coefficient, root mean squared error, and mean absolute error. The results show that RNDv1.0 adequately represents the main characteristics of the measured HONO, and it is thus proposed as a supplementary model for calculating the HONO mixing ratio in a polluted urban environment.

1. Introduction

Surface ozone (O_3) pollution has worsened over continental areas (Arnell et al., 2019;Monks et al., 2015;Varotsos et al., 2013;IPCC, 2014). Particularly, a warmer climate is expected to increase the surface O_3 concentrations and peak levels in polluted regions depending on its precursor levels (IPCC, 2021). As a short-lived climate pollutant (SLCP), O_3 interacts with the global temperature via positive feedback (Shindell et al., 2013;Myhre et al., 2017;Stevenson et al., 2013). Therefore, accurate predictions of the mixing ratios and variations

34 of the surface O_3 are essential. While operational models such as the community multiscale air

35 quality (CMAQ) have been widely used for this purpose, uncertainties still arise from poorly

36 understood chemical mechanisms involving reactive nitrogen oxides (NO_y) and volatile organic

37 compounds (VOCs), and the lack of their measurements (Mallet and Sportisse, 2006;Canty et

38 al., 2015;Akimoto et al., 2019;Shareef et al., 2019;Cheng et al., 2022).

39 In the urban atmosphere, NO_y typically includes NO_x ($NO + NO_2$), HONO, HNO_3,

40 organic nitrates (e.g., PAN), NO_3, N_2O_3, and particulate NO_3^-. These species are produced and

41 recycled through photochemical reactions until they are removed through wet or dry deposition

42 (Liebmann et al., 2018;Brown et al., 2017;Wang et al., 2020;Li et al., 2020). NO_y plays an

43 important role in critical environmental issues concerning the Earth's atmosphere from local air

44 pollution to global climate change (Sun et al., 2011;Ge et al., 2019). The oxidation of NO to

45 NO_2 and finally to HNO_3 is the backbone of the chemical mechanism producing ozone (O_3)

46 and $PM_{2.5}$ (particulate matter with size $\leq$ 2.5 μm), and determines the oxidization capacity of

47 the atmosphere. Recently, as O_3 has still increased even with decreasing NO_x emissions over

48 many regions, including East Asia, interest in the heterogeneous reaction of NO_y, which is yet

49 to be understood, has increased (Brown et al., 2017;Stadtler et al., 2018). Currently, the lack of

50 measurement of individual NO_y species is hindering a comprehensive understanding of the

51 heterogeneous reactions (Anderson et al., 2014;Wang et al., 2017b;Chen et al., 2018b;Akimoto

52 and Tanimoto, 2021;Stadtler et al., 2018).

53 In particular, the evidence for the heterogeneous formation of HONO in relation to high

54 $PM_{2.5}$ and O_3 occurrences in urban areas is increasing (e.g., (Li et al., 2021b)). As an OH

55 reservoir, HONO expedites the photochemical reactions involving VOCs and NO_x in the early

56 morning, leading to O_3 and fine aerosol formation. Nonetheless, its formation mechanism has

57 not been elucidated sufficiently enough to be constrained in conventional photochemical

58 models. In addition to the reaction of NO with OH (Bloss et al., 2021), various pathways of

59 HONO formation have been suggested via laboratory experiments, field measurements, and

60 model simulations: direct emissions from vehicles (Li et al., 2021a) and soil (Bao et al., 2022),

61 photolysis of particulate nitrate (Gen et al., 2022), and heterogeneous conversion of NO_2 on

62 various aerosol surfaces (Jia et al., 2020), ground surface (Meng et al., 2022), and microlayers

63 of the sea surface (Gu et al., 2022). Among these, the heterogeneous reaction mechanism on the

64 surface is of major interest.

HONO has been mostly measured during intensive campaigns in urban areas using various techniques, such as a long path absorption photometer (Kleffmann et al., 2006;Xue et al., 2019), chemical ionization mass spectrometry (Levy et al., 2014;Roberts et al., 2010), ion chromatography (VandenBoer et al., 2014;Gil et al., 2020;Ye et al., 2016;Xu et al., 2019), monitor for aerosols and gases in ambient air (MARGA) (Xu et al., 2019), and quantum cascade - tunable infrared laser differential absorption spectrometry (QC-TILDAS) (Lee et al., 2011;Gil et al., 2021). Among these methods, QC-TILDAS has served as a reference for the intercomparison of measurement data obtained using different techniques due to its high time resolution and stability (Pinto et al., 2014). Previous studies have reported that the maximum HONO of several ppb levels has been observed at nighttime. In comparison, the WRF-Chem and RACM2 model captured approximately 67 %–90 % of the observed HONO in megacities such as Beijing (Tie et al., 2013;Liu et al., 2019).

In recent years, machine learning (ML) methods have been employed in the atmospheric science field for pattern classification (e.g., new particle formation event) and forecasting and spatiotemporal modeling of O_3 and $PM_{2.5}$ (Arcomano et al., 2021;Shahriar et al., 2020;Krishnamurthy et al., 2021;Cui and Wang, 2021;Joutsensaari et al., 2018;Chen et al., 2018a;Kang et al., 2021). Among the ML methods, the neural network (NN) architecture is widely used owing to its powerful ability to process large amounts of data, realizing performance improvement in comparison to the performance of conventional models through integration with physical equations (Reichstein et al., 2019;Schultz et al., 2021). As an NN architecture, a multilayer artificial NN (ANN) that is denoted as a deep NN (DNN) employs a statistical method that learns nonlinear relations in data and yields the optimum solution for the target species without prior information about the physicochemical processes. DNN is more beneficial than other NN architecture, such as convolution NN or long-short term memory, because it works well for discrete spatiotemporal data. Generally, the performance of DNN is similar to or better than that of other ML methods for small as well as large datasets (Baek and Jung, 2021;Dang et al., 2021;Sumathi and Pugalendhi, 2021).

The DNN method requires lots of data to employ it as atmospheric chemical constituent estimation; therefore, the size of the measurement data is a limiting factor for trace species, such as HONO, that are not routinely measured. In this regard, previous studies had been attempted to estimate the daily average HONO mixing ratio by employing ensemble ML models

96   with satellite measurements (Cui and Wang, 2021). Furthermore, a simple NN architecture

97   using ground measurement variables that is believed to be deeply involved in HONO formation,

98   was used to calculate the hourly HONO mixing ratio (Gil et al., 2021). The accuracy of the

99   hourly HONO estimated from input variables, such as aerosol surface areas and mixed layer

100   height, is rated better than the daily HONO estimate.

101   This study aims to develop a user-friendly "reactive nitrogen species simulation using

102   DNN' model (RNDv1.0) that estimates the HONO mixing ratios from the real-time

103   measurements of criteria pollutants and meteorological variables. This study is the first to

104   calculate the HONO mixing ratios using RNDv1.0. The entire construction process is

105   comprehensively described, and the performance is evaluated via comparison with the results

106   of simulations using a commonly used model and observations over several years.

107

108   **2. Model description**

109

110   The RNDv1.0 development follows systematic steps that are similar to a general ML

111   model construction workflow, including data collection, preprocessing data, building the DNN,

112   training, and validating the model, and testing the model performance (Figure 1). RNDv1.0 is

113   written in Python, and the libraries necessary to build and operate RNDv1.0 are listed in Table

114   1. The dataset used to train, test, and validate can be downloaded from Gil et al. (2021).

115

116   **2.1. Collection of measurement data for model construction**

117

118   To construct RNDv1.0, measurement data were obtained, including HONO, reactive

119   gases, and meteorological variables. Note that the HONO measurement data were used for

120   model construction but not required to run the RND model. The HONO mixing ratio was

121   measured in Seoul using a QC-TILDAS system during May–June 2016, June 2018, and April–

122   June 2019 (Lee et al., 2011;Gil et al., 2021), and a MARGA system during May–June 2021 and

123   October–November 2021 (Gil, 2022). When testing and evaluating the atmospheric HONO

124   measurement methods, QC-TILDAS was chosen as the reference method to compare the

ambient HONO mixing ratios measured using several different techniques owing to its advantages of low detection limits (~0.1 ppbv) and high temporal resolution (Pinto et al., 2014). More details on measurements can be found elsewhere (Gil et al., 2021;Gil, 2022).

HONO was measured at the Olympic Park (37.52° N, 127.12° E) during the Korea–United States Air Quality (KORUS-AQ) study in 2016 (Kim et al., 2020;Gil et al., 2021), at the campus of Korea University (37.59° N, 127.03° E) in 2018 and 2021, and at the site near the Korea University campus (37.59° N, 127.08° E) in 2019 (NIER, 2020) (Figure S1). In addition to HONO, trace gases including O_3, NO_2, CO, and SO_2 as well as meteorological variables including temperature (T), relative humidity (RH), wind speed (WS), and wind direction (WD) were measured. Note that HONO was not significantly correlated with any of these variables (Figure S2). The measurement statistics for the entire experimental periods are presented in Table 2 and Table S1. In brief, the 10th and 90th percentile mixing ratios of hourly HONO, NO_2, and O_3, were 0.3 and 2.0 ppbv, 10.0 and 47.0 ppbv, and 8.0 and 75.0 ppbv, respectively.

2.2. Data preprocessing

The observation dataset was prepared for RNDv1.0 model construction. As input variables, hourly measurements of chemical and meteorological variables were used, including the mixing ratios of O_3, NO_2, CO, and SO_2, along with T, RH, WS, WD, and solar zenith angle (SZA) to estimate the target species, HONO, as the output. The WD in degrees was converted to a cosine value for continuity. In the last step of data processing, hourly measurement sets were removed from the input data set if any of the nine variables were missing. Finally, 54.2 % of all the available measurement data (2847) were used to construct and evaluate RNDv1.0.

Since the measurements of the considered nine variables varied over a wide range in different units, they were normalized to avoid bias during the calculations. Among the widely used normalization methods, *min–max scaling* method was adopted, and the input variables were normalized against the minimum and maximum values herein (Eq. 1):

$$x_{sca} = \frac{x_{raw} - F_2(X)}{F_1(X)}, \qquad (Eq.\ 1)$$

where x_{raw} is the raw data, x_{sca} is the scaled value, and the scale factors of F_1 and F_2 correspond to the maximum-minimum and minimum values of the input variable (X), respectively, which are listed in Table 2.

2.3. Neural network architecture and hyperparameters

The network was built using the above input variables to calculate HONO. RNDv1.0 comprises five hidden layers (Figure 2), which employ an exponential linear unit (ELU) as an activation function (Eq. 2).

$$\text{ELU}: \phi(x) = \begin{cases} e^x - 1 \ (x < 0) \\ x \ (x \geq 0) \end{cases}. \qquad \text{(Eq. 2)}$$

In a DNN, an activation function creates a nonlinear relationship between an input variable and an output variable. When constructing a DNN model, ELU affords the advantage of a fast training process and exhibits better performance in handling negative values than other activation functions (Wang et al., 2017a;Ding et al., 2018). Moreover, the mean squared error and Adam optimizer were applied as the loss function and optimization function, respectively. The learning rate, epoch, and batch were set as 0.01, 100, and 32, respectively.

2.4. Model training and k-fold cross validation

RNDv1.0 was trained, validated, and tested with the HONO measurements obtained during May–June 2016 and June 2018, April–June 2019, and May–June 2021 and October–November 2021, respectively (Figure 3). The number of data used for the training and validation was 1122 and that for testing was 1725.

Using the hyperparameters specified in the previous section, the model performance was first validated using the k-fold cross validation (KFCV) method, which is especially useful for small datasets (Bengio and Grandvalet, 2003). In the KFCV method (Figure 3), the entire data are randomly divided into k subsets, of which k − 1 sets are used for training and the remaining one is used for validation. In this study, k was set to 5. The accuracy was determined via index of agreement (IOA), which is expressed as follows (Eq. 3):

$$IOA = 1 - \frac{\sum_{i=1}^{n}(O_i - P_i)^2}{\sum_{i=1}^{n}(|P_i - \bar{O}| + |O_i - \bar{O}|)^2},$$ (Eq. 3)

where O_i, P_i, $\bar{O}$, and n are the observed value, predicted value, average of the observed values, and number of nodes, respectively.

As IOA varies according to the number of nodes, it was calculated for the measured ($HONO_{obs}$) and calculated ($HONO_{mod}$) mixing ratios by varying the number of nodes from 0 to 100 in each hidden layer. The best performance was obtained with 41 nodes, for which the average IOA was 0.89 ± 0.01 (Figure 4). The high IOA value signifies that the performance of RNDv1.0 is adequate, and it is capable of simulating the ambient HONO mixing ratio using the routinely measured criteria pollutants and meteorological variables.

The performance of RNDv1.0 was compared with that of other models, including CMAQv5.3.1 (Appel et al., 2021), random forest (RF), and single-layer ANN (Gil et al., 2021), using the 2016 measurement data. The RF model was constructed using the KFCV method and the same input variables as RNDv1.0 (Figure S4). Its performance was evaluated based on mean absolute error (MAE), root mean square deviation (RMSE), and Pearson correlation coefficient (r):

$$MAE = \frac{\sum_{i=1}^{n}|O_i - P_i|}{n},$$ (Eq. 4)

$$RMSE = \sqrt[2]{\frac{\sum_{i=1}^{n}(O_i - P_i)^2}{n}},$$ (Eq. 5)

$$r = \frac{cov(O,P)}{\sigma_O \sigma_P},$$ (Eq. 6)

208 where σ and *cov* denote the standard deviation and covariance, respectively.

209   All models except CMAQ simulated the measured HONO mixing ratio fairly well
210 (Figure 5). CMAQ not only underestimated the measured HONO but also failed to represent its
211 diurnal variation (Figure 6). The statistical information about the performance of the four
212 models is presented in Table 3. The mean HONO mixing ratio measured and calculated using
213 CMAQ, RF, ANN, and RNDv1.0 was 0.94, 0.09, 0.95, 0.88, and 0.89 ppbv, respectively. Of the
214 four models, RF exhibited the best performance followed by RND. ANN advantageously
215 calculates HONO more accurately than RND as it uses more input variables, but it has a lower
216 data capture rate (41.5 %) compared to RND (97.7 %) or RF (85.3 %).

217

218 **2.5. Model test**

219

220   RNDv1.0 and the RF model were tested using data obtained in June 2018, April 2019,
221 and May–June 2021 and October–November in 2021, which were not used for RNDv1.0
222 training (Figure 3). Note that the RF model outperformed the other three models in the training
223 and validation process (Figure 5). Although the performance of RNDv1.0 was slightly lower
224 than that of the RF model, simulated and measured HONO mixing ratios were in good
225 agreement. Interestingly, the performance of the RF model was much worse than RNDv1.0 in
226 the testing process (Figure 7). The IOA and correlation coefficient of the RF model were
227 extremely low (0.29 and −0.02, respectively).

228   The performance of RNDv1.0 was slightly lower than that of the RF model, but it well
229 traced the HONO mixing ratio. Among the test dataset, the early winter (October–November)
230 data are particularly valuable for demonstrating the applicability of RNDv1.0 because they stem
231 from different weather conditions than the training dataset. For example, HONO mixing ratios
232 reached over 4 ppbv when the daily average $PM_{2.5}$ concentration increased to 120 $\mu g\ m^{-3}$ during
233 severe haze pollution events. Therefore, in the next step, the performance of RNDv1.0 was
234 compared for the two cases by dividing the testing dataset into a group in which all input
235 variables fall within the range of the training dataset and a group which does not meet this

criterion. In RNDv1.0, there was no significant difference in performance between the two groups (Figure S5 and Table S2). When the data in which at least one input variable does not fall within the range of the training dataset were excluded from the test dataset, no significant difference was observed in the performance of RNDv1.0 between the two that meet same atmospheric conditions or do not meet the criteria (Figure S5 and Table S2). These extreme atmospheric conditions can make the model performance be worsened. Except for these extremes, RNDv1.0 well traced the variation of the HONO mixing ratio. These results demonstrate the applicability of RNDv1.0, which is not strictly constrained by atmospheric conditions. The influence of input variable are further analyzed in the next section.

2.6. Bootstrap test and feature importance

A simple bootstrapping test was conducted for both RNDv1.0 and the RF model to evaluate the relative importance of the input variable to the HONO estimates. In this analysis, each variable was set to zero and MAE was calculated as an evaluation metrics (Kleinert et al., 2021). Among the nine input variables of RNDv1.0, NO_2 was found to have the greatest influence on HONO concentration, followed by RH and T (Table 5). The highest MAE of 0.59 ppbv could be considered as the maximum uncertainty of RNDv1.0 due to the input variable. The bootstrap test result well agreed with that of our previous study (Gil et al., 2021), where more variables such as aerosol surface area and mixing layer height were incorporated into the model, it highlights the crucial role of precursor gases and heterogeneous conversion in HONO formation.

In contrast, in the RF model, O_3 was the most important variable. This is likely due to the distinct inverse relationship between O_3 and HONO in the diurnal patterns, and the O_3 variations over a wide range. In conjunction with the evaluation of the test dataset presented in the previous section, the results of the feature importance for the two models demonstrate the ability of RNDv1.0 to simulate the HONO mixing ratio more adequately in urban areas compared to the RF model. Thus, it is reasonable to state that RNDv1.0 constructed using routinely measured criteria pollutants and meteorological variables can sufficiently capture the HONO variability in the urban atmosphere.

3. Operation and application of RNDv1.0

The RNDv1.0 package is provided as an operational model, and the .h5 files that can be opened in Python. To run RNDv1.0, the measurement data for nine input variables are required and needed to be properly prepared, as described in Section 2.2. Once the input data are ready, open RNDv1.0 with the input data files using the code provided in the example (Figure S3). Then, RNDv1.0 calculates and presents the HONO results as scaled values (x_{sca}), which then can be converted to the HONO mixing ratio (ppbv) via the two scale factors shown in Table 2 (Eq. 5):

$$HONO\ (ppbv) = HONO_{sca} \times F_1(HONO) + F_2(HONO). \qquad (5)$$

The HONO calculated using Eq. 5 can be applied to an urban photochemical cycle simulation. As is already known, the photolysis of HONO is a major source of OH radicals in the early morning when the OH level is low, and this OH affects daytime O_3 formation through photochemical reactions with VOCs and NO_x, which are primarily emitted during the morning rush hour in urban areas. Furthermore, the OH produced from HONO promotes the photochemical oxidation of SO_2 and VOCs, leading to aerosol formation. However, the HONO formation mechanism is still poorly understood, which hinders the accurate simulation of O_3 and fine aerosols as well as HONO in conventional photochemical models.

The framework for 0-dimension atmospheric modeling (F0AM), which utilizes the MCM v3.3.1 chemical reaction mechanisms (Wolfe et al., 2016), can be used to simulate the diurnal variation of O_3 with the measurements of several reactive gases (NO, NO_2, CO, HCHO, VOCs, and HONO). Detailed information about F0AM can be found in (https://sites.google.com/site/wolfegm/models) and in previous studies (Wolfe et al., 2016; Gil et al., 2020). When the F0AM model is run without HONO, it is unable to reproduce the concentration and diurnal cycle of the observed O_3 (Figure 8). In comparison, the model well simulates the O_3 within 2 ppbv when HONO is considered, which is the result of RND v1.0.

This is mainly due to the missing OH produced by HONO photolysis in the early morning. Its production rate is estimated to be 0.57 pptv s^{-1}, contributing approximately 2.28 pptv to the OH budget during 06:00–11:00 (Local Sun Time) (Gil et al., 2021). Given that OH is mainly produced from the photolysis of O_3 under high sun, the early morning supply of OH from HONO photolysis will expedite the photochemical cycle involving NO_x and VOCs, promoting O_3 and secondary aerosol formation. The presence of HONO in the photochemical model allows for the accurate estimation of OH radicals; thus, the incorporation of RNDv1.0 into conventional models will improve their overall performance.

4. Summary and implications

In this study, we developed the RND model to calculate the mixing ratio of NO_y in urban atmosphere using a DNN along with measurement data. The target species of RNDv1.0 is HONO, and its mixing ratio is calculated using criteria pollutants, including O_3, NO_2, CO, and SO_2, as well as meteorological variables, including T, RH, WS, WD, and SZA. These variables are routinely measured through monitoring networks. RNDv1.0 was trained and validated using the HONO measurements data obtained in Seoul by adopting a KFCV method and tested with other HONO datasets. The test results demonstrate that RNDv1.0 adequately captures the characteristic variation of HONO.

RNDv1.0 was constructed using the measurements made in a high NO_x environment where the maximum NO_2 reached about 80 ppbv. During the measurement period, the HONO mixing ratio was increased up to about 7 ppb under the influence of air masses originating from China. When applying RNDv1.0 to regions or times heavily affected by transport, the model could possibly underestimate the HONO level without more detailed information, such as nanoparticles. Indeed, a previous study showed that HONO formation is closely related to the surface areas of submicron particles (Gil et al., 2021). Nevertheless, RNDv1.0 is advantageously a relatively inexpensive test for measurement quality control and location selection, and it supports the data used for traditional chemistry models based on the current knowledge of the urban photochemical cycle. Therefore, RNDv1.0 can serve as a supplementary tool for conventional forecasting models. Attempts are currently being made to

estimate ground HONO from satellite observations (Clarisse et al., 2011;Theys et al., 2020;Armante et al., 2021), and RNDv1.0 will be useful for validating the satellite-derived HONO.

5. Acknowledgements

This study was supported by the National Research Foundation of Republic of Korea (2020R1A2C3014592) and Korea Institute of Science and Technology (KIST2E31650-22-P019).

6. Code availability

The RND model codes (.h5 files) with preprocessed sample data can be downloaded from (Gil, 2021).

7. Author contributions

JG and ML designed the manuscript and developed the model code. JK, GL, and JA provided the HONO measurements and CK provided the CMAQ model data. All the authors contributed to the manuscript.

8. Competing interests

The authors declare that they have no conflict of interest.

350 **Figures and Tables**

351

352
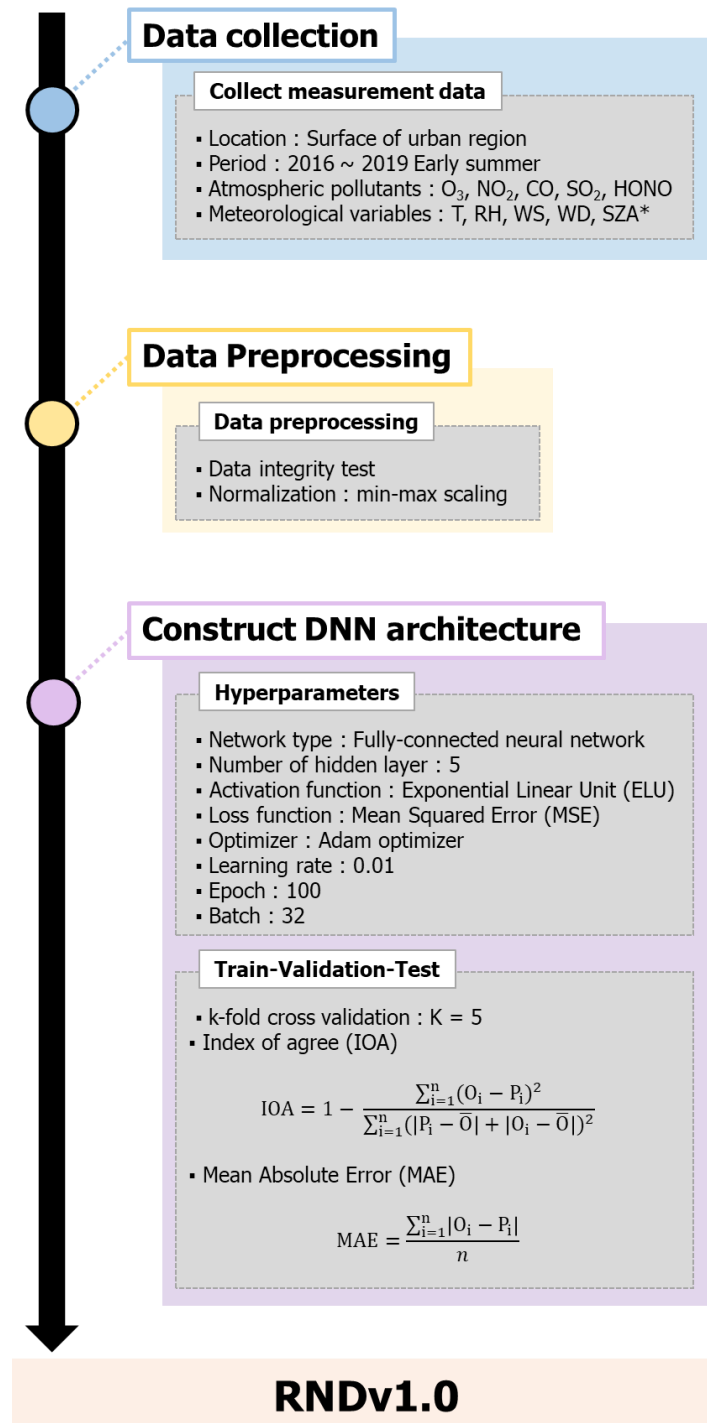
353 **Figure 1.** The main processes for configuring RNDv1.0 (*: calculated values)
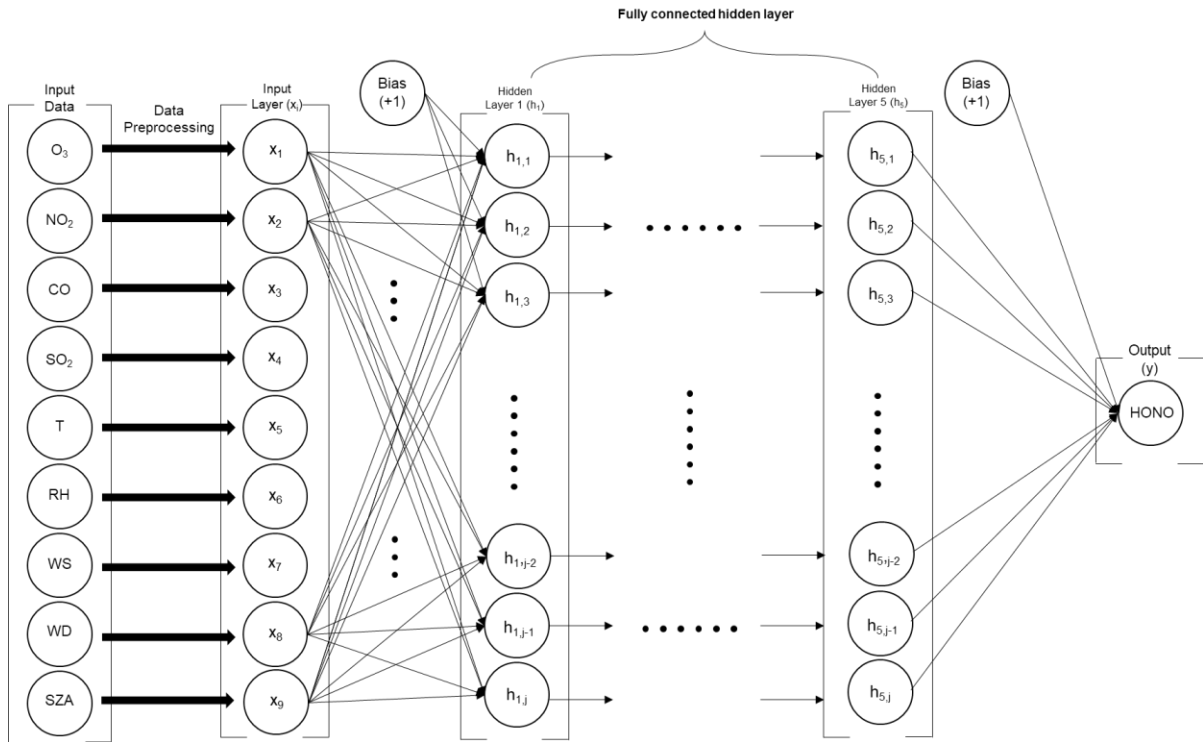
354

355 **Figure 2.** Structure of the deep neural network built for RND v1.0.

356

357
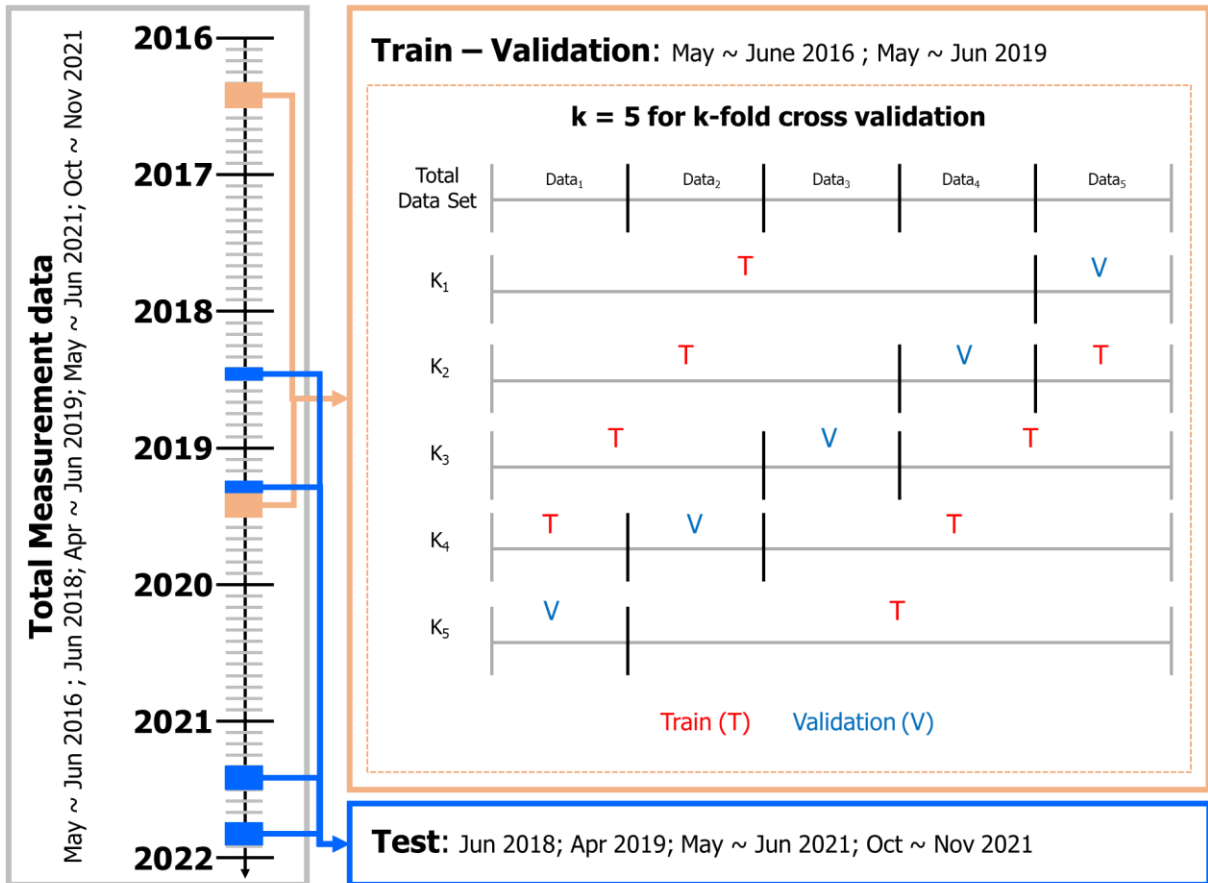
Figure 3. Training, validation, and test design to build RNDv1.0 using the measurement data. The k-fold cross validation was performed using randomly divided five subsets of the training data set.
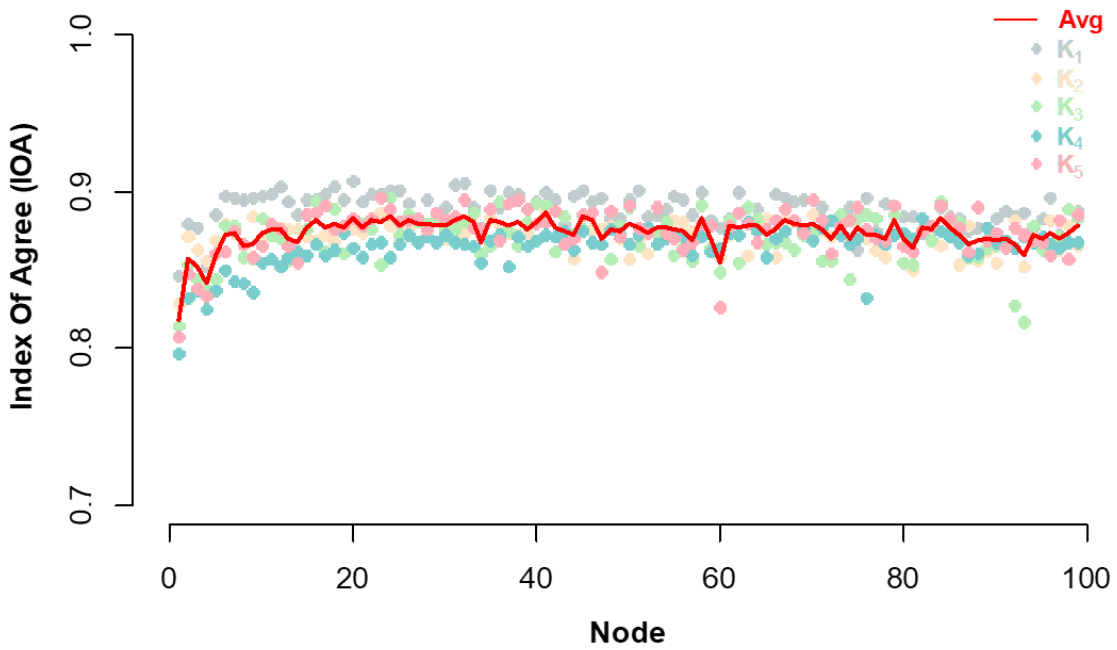
363

364 **Figure 4.** Index of Agreement (IOA) for k-fold cross validation. Solid circle and red line
365 represent IOA for each validation (k = 5) and the average of five validation sets at each node
366 number.

367
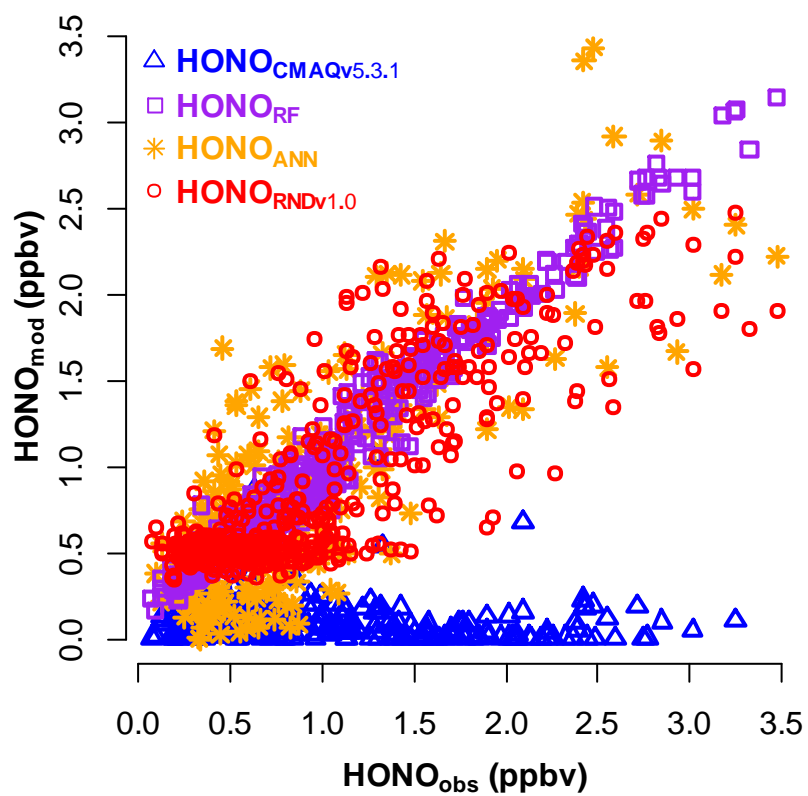
Figure 5. Comparison between the measured HONO (HONO$_{obs}$) and calculated HONO (HONO$_{mod}$) using CMAQv5.3.1 (blue triangle), RF (purple square), ANN (orange star), and RNDv1.0 (red circle) during the KORUS-AQ campaign (May–June 2016).

371

372
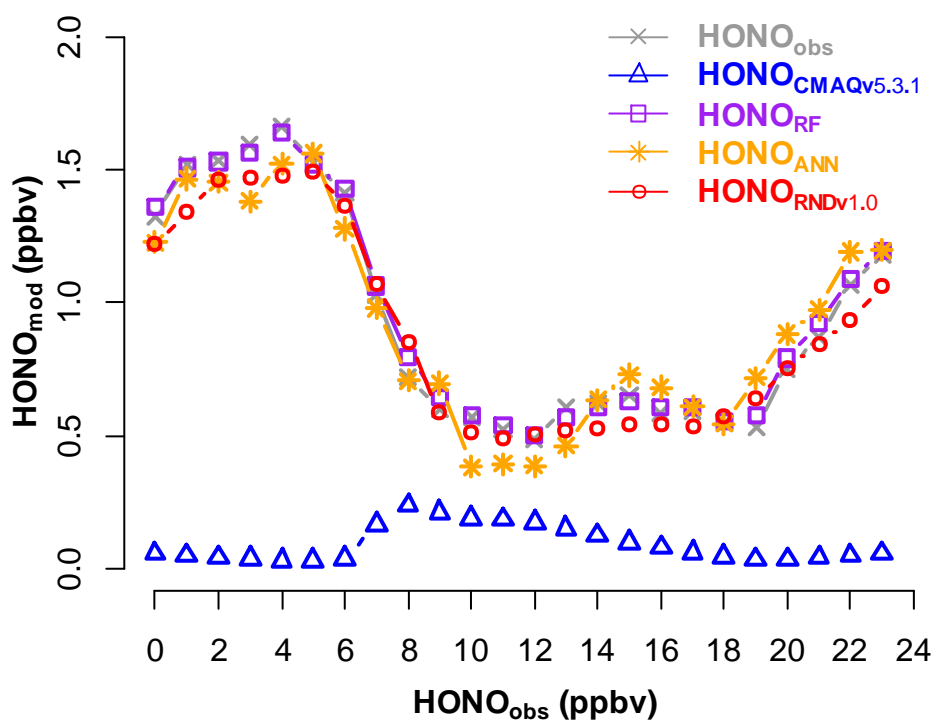
373   **Figure 6**. Average diurnal variation of the measured HONO (HONO$_{obs}$) and calculated

374   HONO (HONO$_{mod}$) using CMAQv5.3.1 (blue triangle), RF (purple square), ANN (orange

375   star), and RNDv1.0 (red circle) during the KORUS-AQ campaign (May–June 2016).

376

377
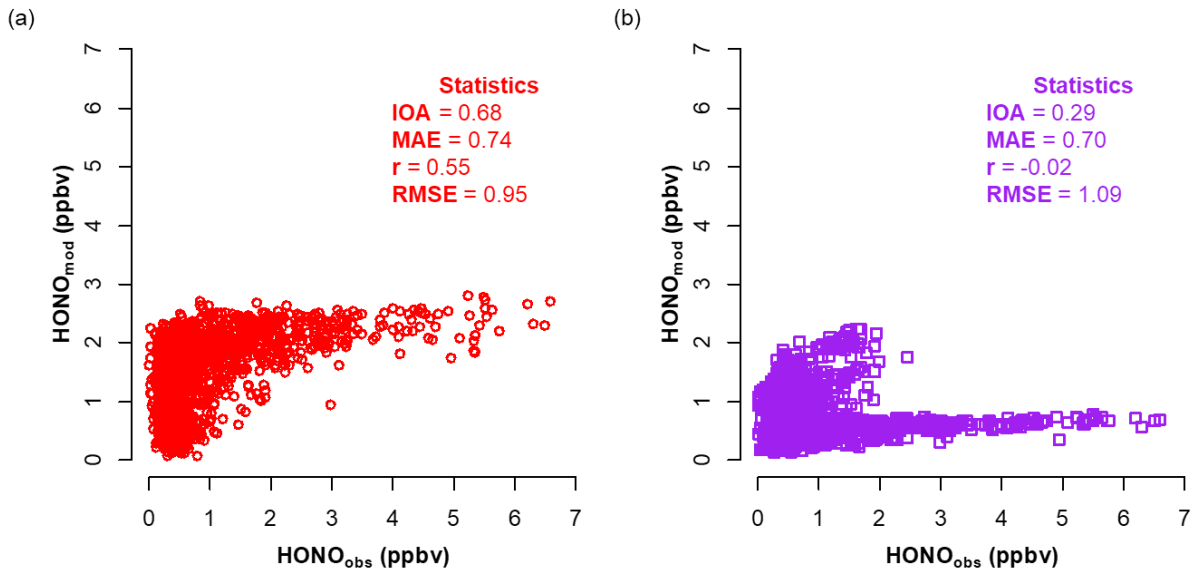
Figure 7. Relationship between measured HONO (HONO$_{obs}$) and modeled HONO (HONO$_{mod}$)

using (a) RNDv1.0 and (b) a Random Forest model for the test dataset.

380

381

382
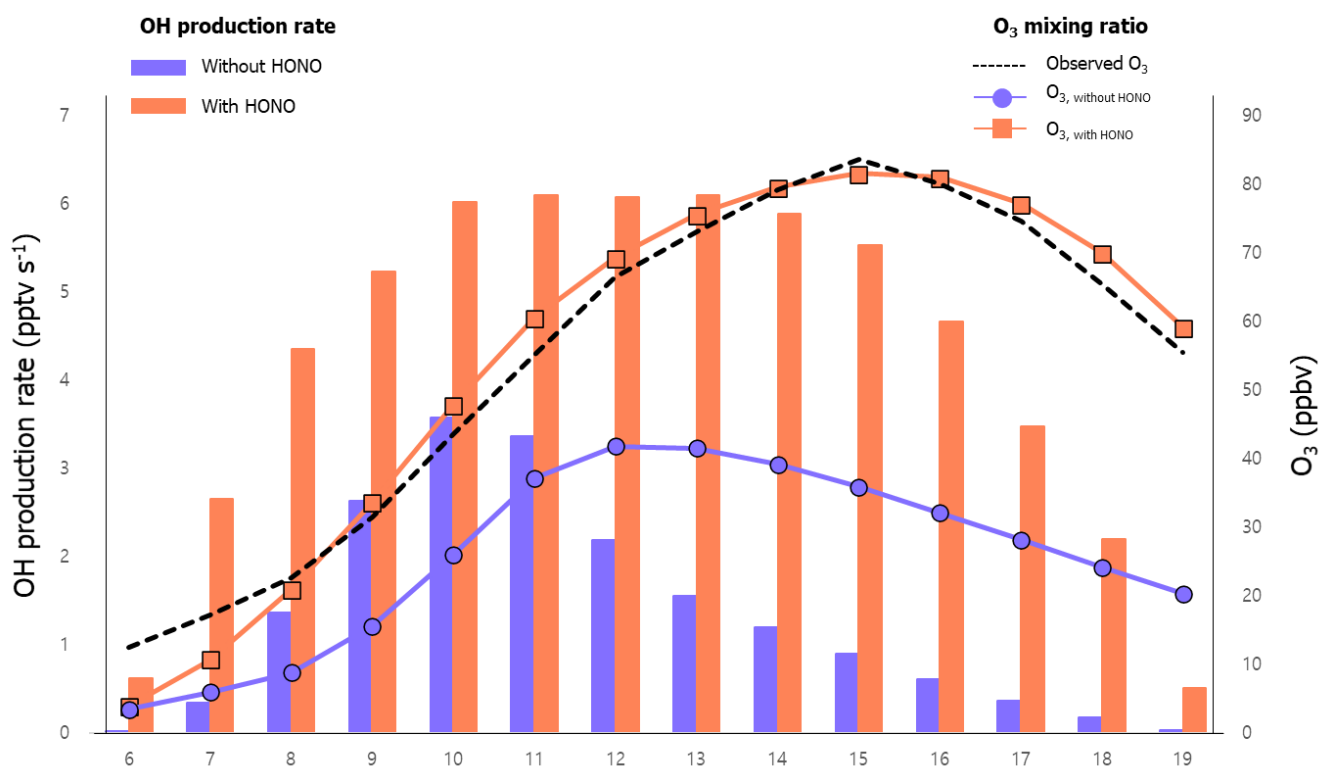
Figure 8. For June 2016, the diurnal variations of O_3 (line) and OH production rate (bar) calculated using the F0AM photochemical model with (orange) and without (blue) HONO estimated from the RNDv1.0 model. The measured and calculated O_3 values are compared.

386

387   **Table 1.** Resources for constructing the RND model.

	Version	Remark
Python	v3.8.3	
CUDA	v10.1	*If using GPU
CuDNN	v7.6.5	*If using GPU
Tensorflow	v2.3.0	*Python library*
Keras	v2.4.3	*Python library*
Pandas	v1.0.5	*Python library*
Numpy	v1.18.5	*Python library*

388   *GPU denotes graphic processing unit

389 **Table 2.** Input variables and their concentrations (10th–90th percentile of the hourly
390 measurements), coverage, and scale factors for the RNDv1.0 model. Measurements were
391 conducted in Seoul during May–June in 2016 and 2019.

	10th–90th percentile (unit)	Coverage (%)	Scale Factor1 (F$_1$)*	Scale Factor 2 (F$_2$)**
Input Variables				
O$_3$	12.1–90.4 (ppbv)	95.5	204.738	0.842
NO$_2$	11.0–48.6 (ppbv)	80.6	79.925	2.375
CO	252–743 (ppbv)	95.1	975.248	137.253
SO$_2$	1.9–6.4 (ppbv)	95.6	12.479	0.958
Solar Zenith Angle	22.7–118.4 (°)	100.0	112.317	14.195
Temperature	15.9–26.7 (℃)	99.4	24.240	8.610
Relative Humidity	29.2–79.1 (%)	99.4	88.545	10.555
Wind Speed	0.2–3.7 (m/s)	99.4	7.581	0.005
Wind Direction	45.4–287.5 (°)	99.4	359.565	0.235
Output Variables				
HONO	0.3–2.0 (ppbv)	81.1 %	3.447	0.013

392 * Maximum–Minimum
393 ** Minimum value

394

395 **Table 3.** Performance of the chemical transport model (CMAQv5.3.1) and machine learning
396 (ML) models, including Random Forest (RF), Artificial Neural Network (ANN), and RNDv1.0,
397 on the measurement data from 2016 KORUS-AQ campaign, which were used for training.

	CMAQv5.3.1	RF	ANN	RNDv1.0
IOA	0.44	0.99	0.86	0.9
r	−0.07	0.99	0.81	0.84
MAE	0.82	0.1	0.38	0.27
RMSE	1.06	0.12	0.41	0.37

398

399

400 **Table 4.** Results of the bootstrap test of measurement data used to train the RF and RNDv1.0

401 models. The greater the MAE, the greater the influence of the variable.

Variable	RF		RNDv1.0	
	MAE	Feature Importance	MAE	Feature Importance
-	0.10	-	0.28	-
O_3	0.57	1	0.29	8
NO_2	0.24	4	0.59	1
CO	0.19	7	0.37	5
SO_2	0.17	8	0.34	6
Solar zenith Angle (SZA)	0.25	2	0.41	4
Temperature (T)	0.21	5	0.52	2
Relative humidity (RH)	0.25	3	0.52	2
Wind speed (WS)	0.20	6	0.34	6
Wind direction (WD)	0.13	9	0.29	8

402

403

Reference

Akimoto, H., Nagashima, T., Li, J., Fu, J. S., Ji, D., Tan, J., and Wang, Z.: Comparison of surface ozone simulation among selected regional models in MICS-Asia III–effects of chemistry and vertical transport for the causes of difference, Atmospheric Chemistry and Physics, 19, 603-615, 2019.

Akimoto, H., and Tanimoto, H.: Review of Comprehensive Measurements of Speciated NOy and its Chemistry: Need for Quantifying the Role of Heterogeneous Processes of HNO3 and HONO, Aerosol and Air Quality Research, 21, 200395, 2021.

Anderson, D. C., Loughner, C. P., Diskin, G., Weinheimer, A., Canty, T. P., Salawitch, R. J., Worden, H. M., Fried, A., Mikoviny, T., and Wisthaler, A.: Measured and modeled CO and NOy in DISCOVER-AQ: An evaluation of emissions and chemistry over the eastern US, Atmospheric Environment, 96, 78-87, 2014.

Arcomano, T., Szunyogh, I., Wikner, A., Pathak, J., Hunt, B. R., and Ott, E.: A Hybrid Approach to Atmospheric Modeling that Combines Machine Learning with a Physics-Based Numerical Model, Journal of Advances in Modeling Earth Systems, e2021MS002712, 2021.

Armante, R., Perrin, A., Kwabia Tchana, F., and Manceron, L.: The v4 bands at 11 μm: linelists for the Trans-and Cis-conformer forms of nitrous acid (HONO) in the 2019 version of the GEISA database, Molecular Physics, e1951860, 2021.

Arnell, N. W., Lowe, J. A., Challinor, A. J., and Osborn, T. J.: Global and regional impacts of climate change at different levels of global temperature increase, Climatic Change, 155, 377-391, 2019.

Baek, W.-K., and Jung, H.-S.: Performance Comparison of Oil Spill and Ship Classification from X-Band Dual- and Single-Polarized SAR Image Using Support Vector Machine, Random Forest, and Deep Neural Network, Remote Sensing, 13, 3203, 2021.

Bao, F., Cheng, Y., Kuhn, U., Li, G., Wang, W., Kratz, A. M., Weber, J., Weber, B., Pöschl, U., and Su, H.: Key Role of Equilibrium HONO Concentration over Soil in Quantifying Soil–Atmosphere HONO Fluxes, Environmental science & technology, 2022.

Bengio, Y., and Grandvalet, Y.: No unbiased estimator of the variance of K-fold cross-validation, Citeseer, 2003.

Bloss, W. J., Kramer, L., Crilley, L. R., Vu, T., Harrison, R. M., Shi, Z., Lee, J. D., Squires, F. A., Whalley, L. K., and Slater, E.: Insights into air pollution chemistry and sulphate formation from nitrous acid (HONO) measurements during haze events in Beijing, Faraday Discussions, 226, 223-238, 2021.

Brown, S. S., An, H., Lee, M., Park, J.-H., Lee, S.-D., Fibiger, D. L., McDuffie, E. E., Dubé, W. P., Wagner, N. L., and Min, K.-E.: Cavity enhanced spectroscopy for measurement of nitrogen oxides in the Anthropocene: results from the Seoul tower during MAPS 2015, Faraday discussions, 200, 529-557, 2017.

Canty, T., Hembeck, L., Vinciguerra, T., Anderson, D., Goldberg, D., Carpenter, S., Allen, D., Loughner, C., Salawitch, R., and Dickerson, R.: Ozone and NO x chemistry in the eastern US: evaluation of CMAQ/CB05 with satellite (OMI) data, Atmospheric Chemistry and Physics, 15, 10965-10982, 2015.

Chen, G., Li, S., Knibbs, L. D., Hamm, N. A., Cao, W., Li, T., Guo, J., Ren, H., Abramson, M. J., and Guo, Y.: A machine learning method to estimate PM2. 5 concentrations across China with remote sensing, meteorological and land use information, Science of the Total Environment, 636, 52-60, 2018a.

Chen, Y., Wolke, R., Ran, L., Birmili, W., Spindler, G., Schröder, W., Su, H., Cheng, Y., Tegen, I., and Wiedensohler, A.: A parameterization of the heterogeneous hydrolysis of N2O5 for mass-based aerosol models: improvement of particulate nitrate prediction, Atmos. Chem. Phys, 18, 673-689, 2018b.

Cheng, P., Pour-Biazar, A., White, A. T., and McNider, R. T.: Improvement of summertime surface ozone prediction by assimilating Geostationary Operational Environmental Satellite cloud observations, Atmospheric Environment, 268, 118751, 2022.

Clarisse, L., R'Honi, Y., Coheur, P. F., Hurtmans, D., and Clerbaux, C.: Thermal infrared nadir observations of 24 atmospheric gases, Geophysical Research Letters, 38, 2011.

Cui, L., and Wang, S.: Mapping the daily nitrous acid (HONO) concentrations across China during 2006-2017 through ensemble machine-learning algorithm, Science of The Total Environment, 147325, 2021.

Dang, C., Liu, Y., Yue, H., Qian, J., and Zhu, R.: Autumn crop yield prediction using data-driven approaches:- support vector machines, random forest, and deep neural network methods, Canadian Journal of Remote Sensing, 47, 162-181, 2021.

Ding, B., Qian, H., and Zhou, J.: Activation functions and their characteristics in deep neural networks, 2018 Chinese control and decision conference (CCDC), 2018, 1836-1841.

Ge, B., Xu, X., Ma, Z., Pan, X., Wang, Z., Lin, W., Ouyang, B., Xu, D., Lee, J., and Zheng, M.: Role of Ammonia on the Feedback Between AWC and Inorganic Aerosol Formation During Heavy Pollution in the North China Plain, Earth and Space Science, 6, 1675-1693, 2019.

460 Gen, M., Liang, Z., Zhang, R., Mabato, B. R. G., and Chan, C. K.: Particulate nitrate photolysis in the atmosphere,
461 Environmental Science: Atmospheres, 2022.
462 Gil, J., Son, J., Kang, S., Park, J., Lee, M., Jeon, E., and Shim, M.: HONO measurement in Seoul during Summer
463 2018 and its Impact on Photochemistry, Journal of Korean Society for Atmospheric Environment, 36, 579-588,
464 10.5572/KOSAE.2020.36.5.579, 2020.
465 Gil, J.: RNDv1.0 and example, https://doi.org/10.5281/zenodo.5540180, in, Zenodo, 2021.
466 Gil, J., Kim, J., Lee, M., Lee, G., Ahn, J., Lee, D. S., Jung, J., Cho, S., Whitehill, A., Szykman, J., and Lee, J.:
467 Characteristics of HONO and its impact on O3 formation in the Seoul Metropolitan Area during the Korea-US Air
468 Quality study, Atmospheric Environment, 2021, https://doi.org/10.1016/j.atmosenv.2020.118182., 2021.
469 Gil, J.: Formation pathways of HONO and its impact on O3 and fine aerosol: based on measurement and modelling
470 study, Doctoral Thesis, 262, 2022.
471 Gu, R., Wang, W., Peng, X., Xia, M., Zhao, M., Zhang, Y., Liu, Y., Shen, H., Xue, L., and Wang, T.: Nitrous acid
472 in the polluted coastal atmosphere of the South China Sea: Ship emissions, budgets, and impacts, Science of The
473 Total Environment, 153692, 2022.
474 IPCC: Summary for policymakers. In: Climate Change 2014: Impacts, Adaption, and Vulnerability. Part A: Global
475 and Sectoral Aspects. Contribution of Working Group II to the Fifth Assessment Report of the Intergovernmental
476 Panel on Climate Change [Field, C.B., V.R. Barros, D.J. Dokken, K.J. Mach, M.D. Mastrandrea, T.E. Bilir, M.
477 Chatterjee, K.L. Ebi, Y.O. Estrada, R.C. Genova, B. Girma, E.S. Kissel, A.N. Levy, S. MacCracken, P.R.
478 Mastrandrea, and L.L.White (eds.)], Cambridge, United Kingdom and New York, NY, USA, 1-32, 2014.
479 Jia, C., Tong, S., Zhang, W., Zhang, X., Li, W., Wang, Z., Wang, L., Liu, Z., Hu, B., and Zhao, P.: Pollution
480 characteristics and potential sources of nitrous acid (HONO) in early autumn 2018 of Beijing, Science of The Total
481 Environment, 735, 139317, 2020.
482 Joutsensaari, J., Ozon, M., Nieminen, T., Mikkonen, S., Lähivaara, T., Decesari, S., Facchini, M. C., Laaksonen,
483 A., and Lehtinen, K. E.: Identification of new particle formation events with deep learning, Atmospheric Chemistry
484 and Physics, 18, 9597-9615, 2018.
485 Kang, Y., Choi, H., Im, J., Park, S., Shin, M., Song, C.-K., and Kim, S.: Estimation of surface-level NO2 and O3
486 concentrations using TROPOMI data and machine learning over East Asia, Environmental Pollution, 288, 117711,
487 2021.
488 Kim, H., Gil, J., Lee, M., Jung, J., Whitehill, A., Szykman, J., Lee, G., Kim, D., Cho, S., Ahn, J., Hong, J., and
489 Park, M.: Overview and characteristics of air quality in the Seoul Metropolitan Area during the KORUS-AQ
490 campaign, Elementa: Science of the Anthropocene, in review, 2020.
491 Kleffmann, J., Lörzer, J., Wiesen, P., Kern, C., Trick, S., Volkamer, R., Rodenas, M., and Wirtz, K.:
492 Intercomparison of the DOAS and LOPAP techniques for the detection of nitrous acid (HONO), Atmospheric
493 Environment, 40, 3640-3652, 2006.
494 Kleinert, F., Leufen, L. H., and Schultz, M. G.: IntelliO3-ts v1.0: a neural network approach to predict near-surface
495 ozone concentrations in Germany, Geoscientific Model Development, 14, 1-25, 2021.
496 Krishnamurthy, R., Newsom, R. K., Berg, L. K., Xiao, H., Ma, P.-L., and Turner, D. D.: On the estimation of
497 boundary layer heights: a machine learning approach, Atmospheric Measurement Techniques, 14, 4403-4424,
498 2021.
499 Lee, B. H., Wood, E. C., Zahniser, M. S., McManus, J. B., Nelson, D. D., Herndon, S. C., Santoni, G., Wofsy, S.
500 C., and Munger, J. W.: Simultaneous measurements of atmospheric HONO and NO 2 via absorption spectroscopy
501 using tunable mid-infrared continuous-wave quantum cascade lasers, Applied Physics B, 102, 417-423, 2011.
502 Levy, M., Zhang, R., Zheng, J., Zhang, A. L., Xu, W., Gomez-Hernandez, M., Wang, Y., and Olaguer, E.:
503 Measurements of nitrous acid (HONO) using ion drift-chemical ionization mass spectrometry during the 2009
504 SHARP field campaign, Atmospheric Environment, 94, 231-240, 2014.
505 Li, S., Song, W., Zhan, H., Zhang, Y., Zhang, X., Li, W., Tong, S., Pei, C., Wang, Y., and Chen, Y.: Contribution of
506 Vehicle Emission and NO2 Surface Conversion to Nitrous Acid (HONO) in Urban Environments: Implications
507 from Tests in a Tunnel, Environmental Science & Technology, 55, 15616-15624, 2021a.
508 Li, Y., Wang, X., Wu, Z., Li, L., Wang, C., Li, H., Zhang, X., Zhang, Y., Li, J., and Gao, R.: Atmospheric nitrous
509 acid (HONO) in an alternate process of haze pollution and ozone pollution in urban Beijing in summertime:
510 Variations, sources and contribution to atmospheric photochemistry, Atmospheric Research, 260, 105689, 2021b.
511 Li, Z., Xie, P., Hu, R., Wang, D., Jin, H., Chen, H., Lin, C., and Liu, W.: Observations of N2O5 and NO3 at a
512 suburban environment in Yangtze river delta in China: Estimating heterogeneous N2O5 uptake coefficients,
513 Journal of Environmental Sciences, 2020.
514 Liebmann, J., Karu, E., Sobanski, N., Schuladen, J., Ehn, M., Schallhart, S., Quéléver, L., Hellen, H., Hakola, H.,
515 and Hoffmann, T.: Direct measurement of NO3 radical reactivity in a boreal forest, Atmospheric Chemistry and
516 Physics, 2018.

517 Liu, Y., Lu, K., Li, X., Dong, H., Tan, Z., Wang, H., Zou, Q., Wu, Y., Zeng, L., and Hu, M.: A comprehensive
518 model test of the HONO sources constrained to field measurements at rural North China Plain, Environmental
519 science & technology, 53, 3517-3525, 2019.

520 Mallet, V., and Sportisse, B.: Uncertainty in a chemistry-transport model due to physical parameterizations and
521 numerical approximations: An ensemble approach applied to ozone modeling, Journal of Geophysical Research:
522 Atmospheres, 111, 2006.

523 Meng, F., Qin, M., Fang, W., Duan, J., Tang, K., Zhang, H., Shao, D., Liao, Z., Feng, Y., and Huang, Y.:
524 Measurement of HONO flux using the aerodynamic gradient method over an agricultural field in the Huaihe River
525 Basin, China, Journal of Environmental Sciences, 2022.

526 Monks, P. S., Archibald, A., Colette, A., Cooper, O., Coyle, M., Derwent, R., Fowler, D., Granier, C., Law, K. S.,
527 and Mills, G.: Tropospheric ozone and its precursors from the urban to the global scale from air quality to short-
528 lived climate forcer, Atmospheric Chemistry and Physics, 15, 8889-8973, 2015.

529 Myhre, G., Aas, W., Cherian, R., Collins, W., Faluvegi, G., Flanner, M., Forster, P., Hodnebrog, Ø., Klimont, Z.,
530 and Lund, M. T.: Multi-model simulations of aerosol and ozone radiative forcing due to anthropogenic emission
531 changes during the period 1990–2015, Atmospheric Chemistry and Physics, 17, 2709-2720, 2017.

532 Pinto, J., Dibb, J., Lee, B., Rappenglück, B., Wood, E., Levy, M., Zhang, R. Y., Lefer, B., Ren, X. R., and Stutz,
533 J.: Intercomparison of field measurements of nitrous acid (HONO) during the SHARP campaign, Journal of
534 Geophysical Research: Atmospheres, 119, 5583-5601, 2014.

535 Reichstein, M., Camps-Valls, G., Stevens, B., Jung, M., Denzler, J., and Carvalhais, N.: Deep learning and process
536 understanding for data-driven Earth system science, Nature, 566, 195-204, 2019.

537 Roberts, J. M., Veres, P., Warneke, C., Neuman, J., Washenfelder, R., Brown, S., Baasandorj, M., Burkholder, J.,
538 Burling, I., and Johnson, T. J.: Measurement of HONO, HNCO, and other inorganic acids by negative-ion proton-
539 transfer chemical-ionization mass spectrometry (NI-PT-CIMS): Application to biomass burning emissions,
540 Atmospheric Measurement Techniques, 3, 981, 2010.

541 Schultz, M., Betancourt, C., Gong, B., Kleinert, F., Langguth, M., Leufen, L., Mozaffari, A., and Stadtler, S.: Can
542 deep learning beat numerical weather prediction?, Philosophical Transactions of the Royal Society A, 379,
543 20200097, 2021.

544 Shahriar, S. A., Kayes, I., Hasan, K., Salam, M. A., and Chowdhury, S.: Applicability of machine learning in
545 modeling of atmospheric particle pollution in Bangladesh, Air Quality, Atmosphere & Health, 13, 1247-1256, 2020.

546 Shareef, M. M., Husain, T., and Alharbi, B.: Studying the Effect of Different Gas-Phase Chemical Kinetic
547 Mechanisms on the Formation of Oxidants, Nitrogen Compounds and Ozone in Arid Regions, Journal of
548 Environmental Protection, 10, 1006-1031, 2019.

549 Shindell, D. T., Lamarque, J.-F., Schulz, M., Flanner, M., Jiao, C., Chin, M., Young, P., Lee, Y. H., Rotstayn, L.,
550 and Mahowald, N.: Radiative forcing in the ACCMIP historical and future climate simulations, Atmospheric
551 Chemistry and Physics, 13, 2939-2974, 2013.

552 Stadtler, S., Simpson, D., Schröder, S., Taraborrelli, D., Bott, A., and Schultz, M.: Ozone impacts of gas–aerosol
553 uptake in global chemistry transport models, Atmospheric chemistry and physics, 18, 3147-3171, 2018.

554 Stevenson, D., Young, P., Naik, V., Lamarque, J.-F., Shindell, D. T., Voulgarakis, A., Skeie, R. B., Dalsoren, S. B.,
555 Myhre, G., and Berntsen, T. K.: Tropospheric ozone changes, radiative forcing and attribution to emissions in the
556 Atmospheric Chemistry and Climate Model Intercomparison Project (ACCMIP), Atmospheric Chemistry and
557 Physics, 13, 3063-3085, 2013.

558 Sumathi, S., and Pugalendhi, G. K.: Cognition based spam mail text analysis using combined approach of deep
559 neural network classifier and random forest, Journal of Ambient Intelligence and Humanized Computing, 12,
560 5721-5731, 2021.

561 Sun, Y., Wang, L., Wang, Y., Quan, L., and Zirui, L.: In situ measurements of SO2, NOx, NOy, and O3 in Beijing,
562 China during August 2008, Science of the Total Environment, 409, 933-940, 2011.

563 Theys, N., Volkamer, R., Müller, J.-F., Zarzana, K. J., Kille, N., Clarisse, L., De Smedt, I., Lerot, C., Finkenzeller,
564 H., and Hendrick, F.: Global nitrous acid emissions and levels of regional oxidants enhanced by wildfires, Nature
565 geoscience, 13, 681-686, 2020.

566 Tie, X., Geng, F., Guenther, A., Cao, J., Greenberg, J., Zhang, R., Apel, E., Li, G., Weinheimer, A., and Chen, J.:
567 Megacity impacts on regional ozone formation: observations and WRF-Chem modeling for the MIRAGE-
568 Shanghai field campaign, Atmospheric Chemistry and Physics, 13, 5655-5669, 2013.

569 VandenBoer, T., Markovic, M., Sanders, J., Ren, X., Pusede, S., Browne, E., Cohen, R., Zhang, L., Thomas, J.,
570 and Brune, W. H.: Evidence for a nitrous acid (HONO) reservoir at the ground surface in Bakersfield, CA, during
571 CalNex 2010, Journal of Geophysical Research: Atmospheres, 119, 9093-9106, 2014.

572 Varotsos, K., Giannakopoulos, C., and Tombrou, M.: Assessment of the Impacts of climate change on european
573 ozone levels, Water, Air, & Soil Pollution, 224, 1-13, 2013.

574 Wang, H., Chen, X., Lu, K., Hu, R., Li, Z., Wang, H., Ma, X., Yang, X., Chen, S., and Dong, H.: NO3 and N2O5
575 chemistry at a suburban site during the EXPLORE-YRD campaign in 2018, Atmospheric Environment, 224,
576 117180, 2020.
577 Wang, T., Qin, Z., and Zhu, M.: An ELU network with total variation for image denoising, International Conference
578 on Neural Information Processing, 2017a, 227-237.
579 Wang, X., Wang, H., Xue, L., Wang, T., Wang, L., Gu, R., Wang, W., Tham, Y. J., Wang, Z., and Yang, L.:
580 Observations of N2O5 and ClNO2 at a polluted urban surface site in North China: High N2O5 uptake coefficients
581 and low ClNO2 product yields, Atmospheric environment, 156, 125-134, 2017b.
582 Wolfe, G. M., Marvin, M. R., Roberts, S. J., Travis, K. R., and Liao, J.: The framework for 0-D atmospheric
583 modeling (F0AM) v3. 1, Geoscientific Model Development, 9, 3309, 2016.
584 Xu, Z., Liu, Y., Nie, W., Sun, P., Chi, X., and Ding, A.: Evaluating the measurement interference of wet rotating-
585 denuder–ion chromatography in measuring atmospheric HONO in a highly polluted area, Atmospheric
586 Measurement Techniques, 12, 6737-6748, 2019.
587 Xue, C., Ye, C., Ma, Z., Liu, P., Zhang, Y., Zhang, C., Tang, K., Zhang, W., Zhao, X., and Wang, Y.: Development
588 of stripping coil-ion chromatograph method and intercomparison with CEAS and LOPAP to measure atmospheric
589 HONO, Science of The Total Environment, 646, 187-195, 2019.
590 Ye, C., Zhou, X., Pu, D., Stutz, J., Festa, J., Spolaor, M., Tsai, C., Cantrell, C., Mauldin, R. L., and Campos, T.:
591 Rapid cycling of reactive nitrogen in the marine boundary layer, Nature, 532, 489-491, 2016.
592